JOURNAL OF SYNCHROTRON RADIATION
ISSN 1600-5775

# Oxidation-induced three-dimensional morphological changes in Ni nanoparticles observed by coherent X-ray diffraction imaging

Kangwoo Ahn,[a,b] In Hwa Cho,[b] Junhyung Kim,[a,b] Su Yong Lee,[b,c] Daeho Sung,[b,d] Chulho Jung,[b,d] Changyong Song,[b,d] Hyon Chol Kang[e] and Do Young Noh[a,b]*

[a]Department of Physics and Photon Science, Gwangju Institute of Science and Technology, Gwangju 61005, Korea, [b]Center for Advanced X-ray Science, Gwangju Institute of Science and Technology, Gwangju 61005, Korea, [c]PAL-XFEL Beamline Division, Pohang Accelerator Laboratory, Pohang 37673, Korea, [d]Department of Physics, Pohang University of Science and Technology, Pohang 37673, Korea, and [e]Department of Materials Science and Engineering, Chosun University, Gwangju 61452, Korea. *Correspondence e-mail: dynoh@gist.ac.kr

Received 21 September 2020
Accepted 6 December 2020

Edited by P. A. Pianetta, SLAC National Accelerator Laboratory, USA

**Keywords:** coherent X-ray diffraction imaging; NiO; three-dimensional morphology; oxidation.

**Supporting information**: this article has supporting information at journals.iucr.org/s

Three-dimensional structures of Ni nanoparticles undergoing significant morphological changes on oxidation were observed non-destructively using coherent X-ray diffraction imaging. The Ni particles were oxidized into $Ni_1O_1$ while forming pores of various sizes internally. For each Ni nanoparticle, one large void was identified at a lower corner near the interface with the substrate. The porosity of the internal region of the agglomerated Ni oxide was about 38.4%. Regions of high NiO density were mostly observed at the outer crust of the oxide or at the boundary with the large voids. This research expands our understanding of general catalytic reactions with direct observation of oxidation-induced nanoscale morphological changes.

## 1. Introduction

Nickel nanoparticles have been utilized in a variety of applications such as catalysts for the reduction process of fuel cells (Faes *et al.*, 2009), energy conversion in solar cells (Karmhag *et al.*, 2000) and hydrogen generation (Chiba *et al.*, 1983; Adkins & Cramer, 1930). Oxidized nickel particles were also investigated extensively as an electrode material based on their porous features (Chuminjak *et al.*, 2017; Cheng *et al.*, 2015). Nickel nanoparticles are easily oxidized due to their large surface area and high reactivity resulting in morphological changes and degrading their performance in various applications. Understanding the oxidation of Ni nanoparticles becomes increasingly important. In nickel nanoparticles, oxidation begins at temperatures below 400°C due to the relatively small activation energy for diffusion compared with their bulk counterparts (Song *et al.*, 2008). Ni nanoparticles smaller than 90 nm are typically oxidized into a nickel oxide shell surrounding a single core pore due to the difference in the atomic diffusion rate between Ni and O atoms as described by the well known Kirkendall effect (Smigelskas & Kirkendall, 1947; Yin *et al.*, 2004). In particles larger than 90 nm, multiple pores are formed during oxidation because the self-diffusion of Ni is impeded by various structural defects, whereas oxygen atoms diffuse easily through nano-sized cracks and grain boundaries present inside Ni particles (Railsback *et al.*, 2010).

The Ni oxidation process has largely been investigated using thermogalvanic analysis (TGA), X-ray diffraction (XRD), scanning electron microscopy (SEM) and transmission electron microscopy (TEM) (Song *et al.*, 2008; Railsback

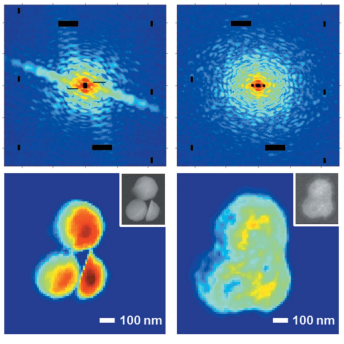

*et al.*, 2010; Kiss *et al.*, 2013; Nakamura *et al.*, 2008; Rellinghaus *et al.*, 2001). TGA and XRD provide information averaged over a whole particle without resolving spatially. On the other hand, SEM and TEM provide complementary local real space information with a high spatial resolution but often limited to two-dimensional (2D) surface or specific sectioned areas. Due to these limitations, it has been difficult to obtain an overall picture of the spatial distributions of the NiO cluster and pore structures.

Coherent X-ray diffraction imaging (CXDI) has become a well established non-destructive probe capable of providing three-dimensional (3D) object density profiles with nanoscale resolution (Chapman *et al.*, 2006; Thibault *et al.*, 2006; Jiang *et al.*, 2010; Takahashi *et al.*, 2010; Kim *et al.*, 2017). In transmission plane-wave CXDI, the electron density of an object projected onto a 2D plane perpendicular to the incident coherent X-ray beam direction is reconstructed using various phase-retrieval algorithms from the corresponding diffraction patterns in the small-angle regime together with object constraints (Fienup, 1982; Miao *et al.*, 1998, 2003, 2012). The diffraction data recorded onto a 2D detector represent only the magnitude of the diffracted X-ray field, and the phase information, that is essential to reconstruct a sample image, is lost. Overcoming the sample isolation constraint imposed on the CXDI by scanning an X-ray beam across a sample area using the ptychography principle, the ptychographic CXDI has increased its application areas greatly (Thibault *et al.*, 2008; Maiden & Rodenburg, 2009).

Several iterative algorithms, such as Error Reduction (ER) (Fienup, 1982), Hybrid Input Output (HIO) (Fienup, 1982) and Guided Hybrid Input Output (GHIO) (Chen *et al.*, 2007), have been proposed for retrieving the lost phase of the diffracted X-ray field utilizing a priori object information in real space. Since the complex diffracted X-ray field represents the Fourier transform of an object electron density in the Born approximation, which is valid for most nanoscale objects, a real space object image can be reconstructed by Fourier inverse-transforming the diffraction field. The spatial resolution of this phase-contrast-based 2D CXDI has often been limited by the weak diffraction signal at large diffraction angles but has continuously been improved to a few nanometres (Miao *et al.*, 2015; Kim *et al.*, 2014).

In addition, a 3D electron density map of the object can be produced by applying computed tomography (CT) principles to a number of 2D reconstructed images obtained at different object angles relative to the incident X-ray beam direction. The biggest advantage of 3D CXDI is the capability of investigating the internal structure of an object non-destructively. In most cases, the spatial resolution of the 3D CXDI is still limited to tens of nanometres which is far from resolving individual atoms (Gallagher-Jones *et al.*, 2016). However, 3D CXDI has demonstrated great potential in investigating materials processes involved in catalytic reactions, alloying, dewetting and so forth in a non-destructive manner (Robinson *et al.*, 2016; Liu *et al.*, 2018; Kim *et al.*, 2019, 2020).

In this paper, we present a morphological analysis of Ni particles before and after oxidation by reconstructing 3D electron density maps using the 3D CXDI technique quantitatively. Ni nanoparticles were converted into $Ni_1O_1$ and agglomerated during oxidation. Inside each Ni particle, one large void stemming from the substrate was observed. NiO regions were unevenly mixed with pores which were mostly unresolved due to the limited spatial resolution. High-density NiO regions were located at the outer crust of the oxide or the boundary with the large voids formed inside each Ni particle.

## 2. Sample preparation and experiment setup

### 2.1. Preparation of Ni nanoparticles

The thin film dewetting process (Petersen & Mayr, 2008; Gentili *et al.*, 2012) was employed to prepare crystalline Ni nanoparticles. After depositing a Ni film on the sapphire substrate using an electron beam evaporator to a thickness of about 30 nm, it was annealed for 6 h at 1050°C in a tube furnace under a vacuum of $10^{-6}$ Torr. As a result of the dewetting, hemispherical Ni nanoparticles of 200 to 500 nm size were formed on the substrate that were highly crystalline as confirmed by X-ray diffraction measurement.

A CXDI measurement requires a sample object to be isolated and well confined inside the coherent volume of the X-ray beam to fulfill the oversampling requirement (Miao *et al.*, 1998). It is also important to ensure that signals from nearby objects or substrate do not mix when rotating the sample object for 3D measurements. For this purpose, we detached the Ni nanoparticles from the sapphire substrate by stirring them in an ultrasonic cleaner and scraping with clean Teflon tweezers, and mixed into ethanol solvent. After diluting the solution to a suitable level, the solution was sprayed on a 50 nm-thick $Si_3N_4$ membrane, which is mostly X-ray transparent, and dried. Among the Ni nanoparticles left on the membrane, we chose a sample object composed of three Ni nanoparticles that provided an oversampling ratio of 5 to 10 to facilitate the phase retrieval from the diffraction signal. We ensured that no other particles exist within 50 µm of the sample object center. After completing the 3D CXDI measurement for the original Ni nanoparticles, the nanoparticles were annealed at 500°C in air for two hours for complete oxidation following previous reports (Railsback *et al.*, 2010).

### 2.2. Coherent X-ray diffraction measurement procedure

The CXDI experiment was carried out at the 9C undulator beamline at Pohang Light Source II in Korea. The energy of X-rays was set to 5.6 keV (2.21 Å) optimized for the coherent beam flux at the beamline. The X-ray beam was focused using a Kirkpatrick–Baez (KB) mirror to 14 µm (horizontal) × 9 µm (vertical) at the sample position. Two slits were installed in front of the sample to reduce parasitic scattering generated as the main X-ray beam passes through the beamline optical components. The diffracted X-ray signal of the sample was acquired with a 2D detector (PILATUS 1M, pixel size 172 µm × 172 µm, 1043 × 981 pixels). We used only the data in the central 500 × 500 pixels with a reasonable signal-to-noise

ratio. To prevent damage to the detector due to the intense direct X-ray beam, a beam stop was installed in front of the detector. The distance between the sample and the detector, which determines the speckle size and oversampling ratio, was 5 m.

To obtain diffraction patterns at various incident angles required for 3D tomographic reconstruction, samples were rotated around the vertical axis perpendicular to the incident X-ray beam direction. The angular interval and the number of 2D diffraction patterns affect the image resolution as well as the measurement time. We followed the equally sloped tomography (EST) scheme (Miao *et al.*, 2005) to determine an optimal angular interval. The EST scheme provides a uniform 3D diffraction pattern with optimal number of rotation angles maintaining resolution and minimizing radiation damage.

We obtained a diffraction pattern for a total of 28 angles over the range of rotation $\pm 76^{\circ}$. The time taken to obtain the whole diffraction patterns for a 3D image reconstruction was about 16 minutes. The data acquisition time at a given angle was mostly determined by the intensity level of the sample signal. After measuring the diffraction data of the sample at each angle, the background noise was measured and subtracted.

### 2.3. Phase retrieval procedure

In order to retrieve the phase from the measured X-ray diffraction amplitude, we employed the HIO algorithm with the assumption that the sample was isolated within a specific region called the support. Although a loosely defined support is sufficient for the retrieval, it is often necessary to find an optimal support in the case of an object with a complicated structure. In this study, we applied the shrinkwrap method (Marchesini *et al.*, 2003) repeatedly to determine the optimal support to the reconstructed images obtained with the HIO algorithm (Fienup, 1982). The ten best images obtained with an optimized support were averaged to determine the final 2D projected image at a given object angle. This procedure was applied equally to the diffraction patterns obtained at all 28 angles.

## 3. Results and discussion

### 3.1. 2D projection image analysis

Fig. 1 shows the 2D coherent X-ray diffraction patterns obtained keeping the substrate normal parallel to the incident X-ray direction together with the corresponding reconstructed projection images of the Ni particles before and after oxidation. The centro-symmetry approximation in the diffraction pattern of a real value object was applied to fill the unmeasured portions due to the beam stop and the gap in the detector. While the diffraction pattern of the Ni particles in Fig. 1(*a*) exhibits streaky features indicating the presence of sharp surfaces in the Ni particles, the pattern after oxidation is more speckly without streaks, which is a signature of a disordered object with roughened surface.

The reconstructed 2D CXDI images illustrated in Figs. 1(*c*) and 1(*d*) show that three distinct Ni particles have oxidized into a large oxide cluster with rounded surface during annealing. The spatial resolution of the CXDI images estimated from the phase retrieval transfer function (PRTF) (Chapman *et al.*, 2006) is 13 nm for the Ni particles and 17 nm for the oxidized cluster. Both images of the sample before and after oxidation exhibit a quite similar shape to the corresponding SEM images shown in the insets.

The 2D CXDI images, which represent quantitative electron density maps of the particles integrated along the incident X-ray direction, however, provide additional information about the internal features which is not clearly visible in the SEM images. Most importantly, as shown in Fig. 1(*d*), the projected density of the oxidized Ni is not uniform suggesting

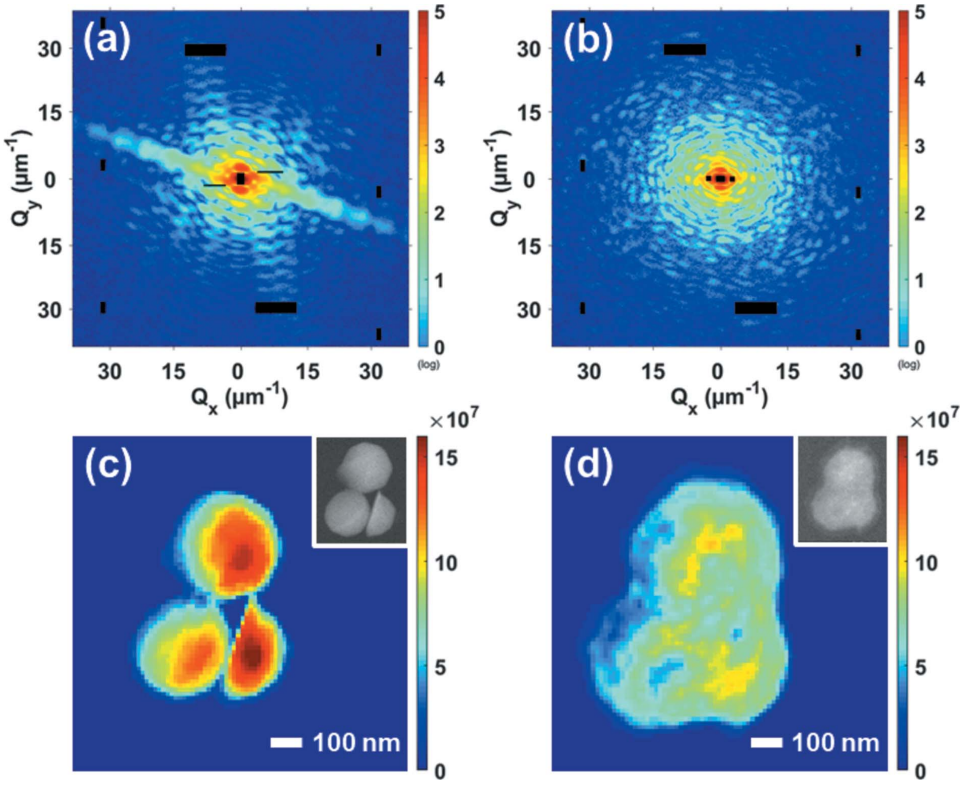


**Figure 1**
2D coherent X-ray diffraction patterns before (*a*) and after oxidation (*b*) of three agglomerated Ni nanoparticles. The black boxed areas represent the gaps between the images sensors, dead pixels and the beam-stop area, and the data inside were not used in the reconstruction. (*c*, *d*) 2D projection CXDI image reconstructed using the diffraction amplitude shown in (*a*, *b*), respectively. The insets show the corresponding SEM images.

the existence of voids or pores inside or various oxidation states. The total number of electrons comprising the sample object before and after oxidation can quantitatively be estimated from the 2D projection images using (Kim *et al.*, 2017)

$$N_e^2 = \frac{I(0)}{I_0 r_e^2 \, d\Omega}, \qquad (1)$$

where $N_e$ is the number of total electrons interactiong with the X-rays, $I(0)$ is the number of diffracted X-ray photons as a value of the center pixel of the reconstructed diffraction pattern, $I_0$ is the incident X-ray flux, $r_e$ is the classical electron radius, and $d\Omega$ is the solid angle covered by the pixel. $I_0$ was evaluated from the measured photo-current using a photo-diode for the main beam prior to the CXDI measurement.

The incident X-ray flux $I_0$ used in the measurement of the specimen before and after oxidation was $3.86 \times 10^8$ and $4.91 \times 10^8$ photons $\mu m^{-2} s^{-1}$, respectively. The total number of electrons of the Ni particles thus obtained was $1.19 \times 10^{11}$ that increased to $1.54 \times 10^{11}$ during oxidation. The increase of electrons by 29.4% during oxidation is in good agreement with the formation of $Ni_1O_1$ from Ni. The number of electrons in a NiO molecule is about 28.6% larger than in Ni. We conclude that the Ni nanoparticles were mostly oxidized into $Ni_1O_1$ under the oxidation condition employed in this study, although the resultant oxide was not compact. It was, however, not possible to describe details of the internal morphology using the 2D CXDI image, which called for a 3D analysis.

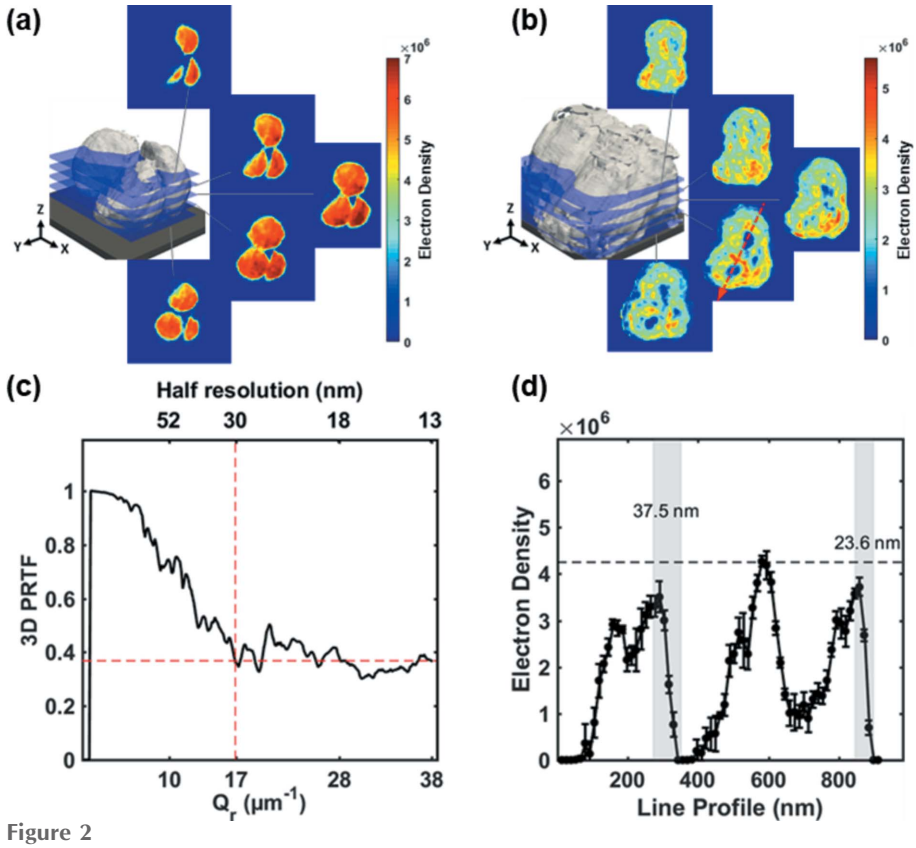


**Figure 2**
(*a*, *b*) 3D surface rendered images and cross-section images of the Ni particles before (*a*) and after (*b*) oxidation. In the rendered images, the surface was defined at 20% of the maximum value. The interval between the cross section is 52 nm. (*c*) 3D phase retrieval transfer function (PRTF) of the reconstruction of the Ni particles before and after oxidation. (*d*) Line profile of the electron density along the path indicated in (*b*) by the red dotted arrow. The black dashed line is the electron density of compact $Ni_1O_1$.

### 3.2. 3D tomographic image analysis

Shown in Figs. 2(*a*) and 2(*b*) are the reconstructed 3D electron density images before and after oxidation obtained by applying the CT method on the 2D projected images obtained at the 28 angles provided by the EST scheme. To avoid the problems associated with the fluctuations in the incident X-ray intensity, the projected electron density map at each angle was normalized to yield the same total electron density. Each 2D reconstructed image was composed of 500 × 500 pixels, and the spatial dimensions of a unit voxel of the 3D image were 13 nm × 13 nm × 13 nm. All reconstructed 2D images are shown in the supporting information (Figs. S1 and S2).

The morphology of the Ni particles changed drastically in all three dimensions during oxidation. The volume of the oxidized Ni increased and the sharp surfaces were rounded as indicated in the surface rendered image.

The cross-sectional images shown in Figs. 2(*a*) and 2(*b*) were prepared by slicing the Ni particles and the oxidized Ni particles parallel to the substrate computationally with a 52 nm interval. Each image illustrates the voxel electron density map of the surface of a slice that provides a view of the internal density distribution of oxidized Ni particles. The as-prepared specimen was composed of three Ni hemispherical nanoparticles all in contact with the substrate as illustrated in Fig. 2(*a*).

The density of the as-prepared particles was about $9.0 \pm 1.2$ g cm$^{-3}$, close to the ideal Ni density (8.91 g cm$^{-3}$), and was relatively uniform compared with after oxidation in 3D as shown in the cross-sectional images. The cross-sectional views of the oxidized Ni in Fig. 2(*b*) show that the density is uneven and there exist large voids extending from the substrate.

The formation of voids is attributed to the difference in the Ni self-diffusion and Ni–NiO diffusion coefficient as reported by Nakamura *et al.* (2008), which explains vacancy migration and pore formation during the oxidation process. The vacancies have sufficient mobility to migrate and aggregate into pores and voids. The formation of large voids near the

substrate indicate that the diffusion of Ni atoms was hindered by the substrate and they diffuse preferentially upward away from the substrate to form NiO. The large void in the oxide near the center is connected to the empty space between the as-prepared Ni particles.

We estimated the spatial resolution (half resolution) of the 3D images by using the 3D PRTF together with the line profile at steeply varying regions in the images. The resolution in the oxide image estimated from the 3D PRTF shown in Fig. 2(*c*) was about 30 nm. Fig. 2(*d*) shows a line profiles across the voids indicated by a red arrow, which illustrates that the electron density changes rapidly within two or three pixels. We estimate that the image resolution especially near sharp edges is also close to 30 nm, similar to the value estimated from the 3D PRTF.

The density of the oxidized Ni was highly non-uniform as illustrated in the cross-sectional views; some parts having values close to the full compact NiO density but most regions with a much lower value. This indicates that there exist invisible multiple small pores (Railsback *et al.*, 2010; Medford *et al.*, 2013) in addition to the visible voids mixed into NiO that are not distinguishable due to the limited resolving power of the 3D CXDI employed here.

The electron density of most voxels was lower than the compact NiO electron density. Shown in Fig. 3 is the histogram of voxels sorted according to the electron density of the oxidized Ni, which exhibits its maximum near 60% of compact NiO density. We counted only the voxels internal to the volume occupied by the as-prepared Ni particle aggregate shown in Fig. 2(*a*) to remove the uncertainty in the voxels near the boundary whose density value is not well defined. Since each Ni atom is completely oxidized into $Ni_1O_1$, as we confirmed by the increase in the total number of electrons during oxidation, the ratio of the electron density of a voxel to the compact NiO density represents the fraction of the voxel space filled with NiO. The other part is presumably occupied by a single pore or multiple pores smaller than the resolution limit. The porosity, the ratio of pore space, of the internal region evaluated using the histogram is 38.4%. Although these small pores were not distinguished due to the limited resolution employed here, the histogram analysis of the reconstructed 3D image indicates a multi-pored structure in which small pores are unevenly mixed with the NiO clusters in the oxide. Railsback *et al.* (2010) reported that multi-pore NiO is formed due to defects such as grain boundaries, dislocations and cracks that act as oxygen diffusion channels in Ni particles larger than 90 nm.

Fig. 4(*a*) shows top and side views of the observable voids (or large pores) formed during oxidation with reference to the position of the original as-prepared Ni nanoparticles which is indicated by the red nets. The reconstructed 3D image of the as-prepared Ni specimen was positioned with respect to the image of the oxidized specimen by aligning their center of mass position in the *X* and *Y* directions. In the *Z*-direction, the substrate position was used as the reference point. First, we note that a single large void was formed in each particle, which is also supported in the cross-sectional images shown in Fig. 2(*b*). It is also well illustrated in a movie made of more sectioned images along the substrate normal (Movie S1 of the supporting information). The size of the large void was about 100 nm. As discussed previously, the fast Ni self-diffusion rate

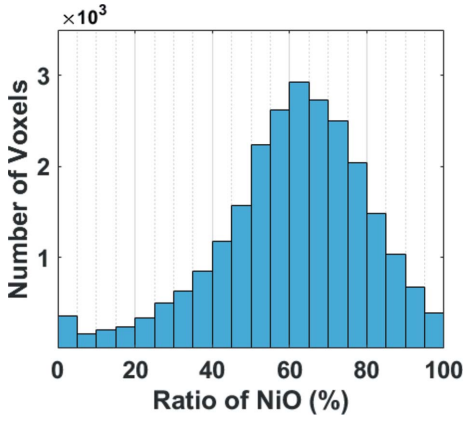


**Figure 3**
Histogram of the electron density of the oxidized Ni particle in the region internal to the volume occupied by the as-prepared Ni particle aggregate. The value of the abscissa represents the percentage of the compact NiO in a voxel.

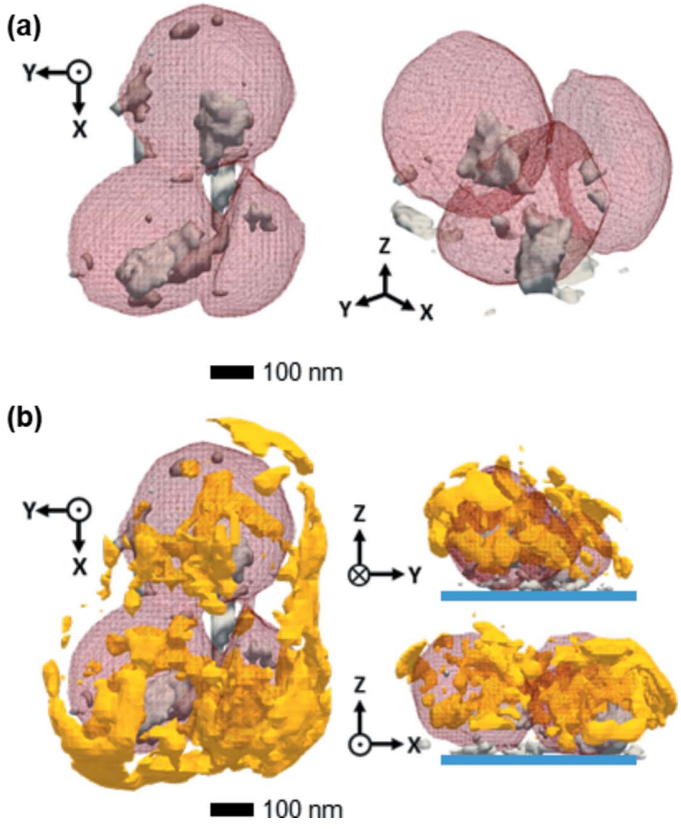


**Figure 4**
(*a*) Top and side views of the 3D rendered image of voids (gray regions, under of 20% NiO density) of the oxidized Ni particles. The red-meshed region represents the space that used to be occupied by the Ni particles before oxidation. We note that the voids were mainly formed inside the original Ni particles. (*b*) Regions with electron density over 80% NiO density shown as yellow crust.

facilitates the subsequent vacancy migration resulting in the formation of large voids. Since the diffusion of Ni towards the substrate is relatively small, Ni atoms preferentially diffuse away from the substrate and the voids locate near the bottom. The growth of the voids is inhibited by the NiO formed by the oxygen diffused through defects. There also exist smaller isolated observable voids of size less than 50 nm, most of which were formed inside the original Ni particles. Only a few voids were found outside the region occupied by the original Ni particles. This indicates that the observable voids were essentially formed as Ni atoms diffused out of the Ni particles to form oxide.

Finally, we illustrate the region of compact NiO, which we define as the area with density over 80% of NiO density using a 3D rendering program, in Fig. 4(*b*). The compact NiO region comprises mostly an outer crust partially enclosing the oxidized particle and an inner region enclosing the three large voids. However, the NiO crust is not continuous and does not form a complete shell. We conjecture that the outer crust was formed by the Ni atoms diffused out through the inner Ni regions to meet oxygen outside the particles. The compact NiO regions formed inside the original particle boundary were supposedly formed by the oxygen diffused through defects that meets Ni atoms. Since the Ni atoms do not diffuse much once they are oxidized into NiO, the inner NiO parts would limit the growth of the voids and thus enclose the voids.

## 4. Conclusion

Quantitative 3D electron density maps of Ni nanoparticles before and after oxidation were successfully reconstructed using CXDI non-destructively. Three Ni nanoparticles fused into an enlarged oxide cluster that was composed of nickel oxide and multiple pores. The chemical composition of the nickel oxide turned out to be $Ni_1O_1$ as revealed from the increase in the total number of electrons. A single large void, about 100 nm in size, was formed inside each Ni particle, and most of the observable voids reside inside the boundary of the as-prepared Ni particles. The porosity of the internal region of the agglomerated Ni oxide was about 38.4%. On the other hand, most of the pores were not distinguishable due to the limited resolution of about 30 nm, and mixed unevenly with NiO. Information on the changes in 3D morphology and pore structure during oxidation of Ni nanoparticles would be valuable in understanding their catalytic functions. With further improvement in image resolution and *in situ* capabilities, 3D CXDI, which can be applied under ambient conditions different from most electron microscopies, can be a powerful probe for investigating materials processes non-destructively and understanding the functionality of nanoscale materials in relation to their 3D morphology.

## Acknowledgements

We acknowledge valuable contributions of Hojun Oh and Ouyoung Kwon in data collection.

## Funding information

Funding for this research was provided by: National Research Foundation of Korea (grant No. 2015R1A5A1009962); Gwangju Institute of Science and Technology (grant No. 2020).This research was supported by the National Research Foundation of Korea (NRF) grant funded by the Korea government(MSIT) (No. 2015R1A5A1009962), and by a GIST Research Institute(GRI) grant in 2020.

## References

Adkins, H. & Cramer, H. I. (1930). *J. Am. Chem. Soc.* **52**, 4349–4358.
Chapman, H. N., Barty, A., Marchesini, S., Noy, A., Hau-Riege, S. P., Cui, C., Howells, M. R., Rosen, R., He, H., Spence, J. C. H., Weierstall, U., Beetz, T., Jacobsen, C. & Shapiro, D. (2006). *J. Opt. Soc. Am. A*, **23**, 1179–1200.
Chen, C.-C., Miao, J., Wang, C. W. & Lee, T. K. (2007). *Phys. Rev. B*, **76**, 064113.
Cheng, J., Zhao, B., Zhang, W., Shi, F., Zheng, G., Zhang, D. & Yang, J. (2015). *Adv. Funct. Mater.* **25**, 7381–7391.
Chiba, T., Okimoto, M., Nagai, H. & Takata, Y. (1983). *Bull. Chem. Soc. Jpn*, **56**, 719–723.
Chuminjak, Y., Daothong, S., Kuntarug, A., Phokharatkul, D., Horprathum, M., Wisitsoraat, A., Tuantranont, A., Jakmunee, J. & Singjai, P. (2017). *Electrochim. Acta*, **238**, 298–309.
Faes, A., Nakajo, A., Hessler-Wyser, A., Dubois, D., Brisse, A., Modena, S. & Van herle, J. (2009). *J. Power Sources*, **193**, 55–64.
Fienup, J. R. (1982). *Appl. Opt.* **21**, 2758–2769.
Gallagher-Jones, M., Rodriguez, J. A. & Miao, J. (2016). *Q. Rev. Biophys.* **49**, e20.
Gentili, D., Foschi, G., Valle, F., Cavallini, M. & Biscarini, F. (2012). *Chem. Soc. Rev.* **41**, 4430–4443.
Jiang, H., Song, C., Chen, C.-C., Xu, R., Raines, K. S., Fahimian, B. P., Lu, C.-H., Lee, T.-K., Nakashima, A., Urano, J., Ishikawa, T., Tamanoi, F. & Miao, J. (2010). *Proc. Natl Acad. Sci. USA*, **107**, 11234–11239.
Karmhag, R., Tesfamichael, T., Wäckelgård, E., Niklasson, G. A. & Nygren, M. (2000). *Solar Energy*, **68**, 329–333.
Kim, C., Kim, Y., Kim, S. S., Kang, H. C., McNulty, I. & Noh, D. Y. (2014). *Opt. Express*, **22**, 5528–5535.
Kim, D., Chung, M., Kim, S., Yun, K., Cha, W., Harder, R. & Kim, H. (2019). *Nano Lett.* **19**, 5044–5052.
Kim, Y., Kim, C., Ahn, K., Choi, J., Lee, S. Y., Kang, H. C. & Noh, D. Y. (2020). *J. Synchrotron Rad.* **27**, 725–729.
Kim, Y., Kim, C., Kwon, O. Y., Nam, D., Kim, S. S., Park, J. H., Kim, S., Gallagher-Jones, M., Kohmura, Y., Ishikawa, T., Song, C., Tae, G. & Noh, D. Y. (2017). *Sci. Rep.* **7**, 1850.
Kiss, A. M., Harris, W. M., Wang, S., Vila-Comamala, J., Deriy, A. & Chiu, W. K. S. (2013). *Appl. Phys. Lett.* **102**, 053902.
Liu, X., Lin, W., Chen, B., Zhang, F., Zhao, P., Parsons, A., Rau, C. & Robinson, I. (2018). *Mater. Des.* **157**, 251–257.
Maiden, A. M. & Rodenburg, J. M. (2009). *Ultramicroscopy*, **109**, 1256–1262.
Marchesini, S., He, H., Chapman, H. N., Hau-Riege, S. P., Noy, A., Howells, M. R., Weierstall, U. & Spence, J. C. H. (2003). *Phys. Rev. B*, **68**, 140101.
Medford, J. A., Johnston-Peck, A. C. & Tracy, J. B. (2013). *Nanoscale*, **5**, 155–159.
Miao, J., Amonette, J. E., Nishino, Y., Ishikawa, T. & Hodgson, K. O. (2003). *Phys. Rev. B*, **68**, 012201.
Miao, J., Förster, F. & Levi, O. (2005). *Phys. Rev. B*, **72**, 052103.
Miao, J., Ishikawa, T., Robinson, I. K. & Murnane, M. M. (2015). *Science*, **348**, 530–535.
Miao, J., Sandberg, R. L. & Song, C. (2012). *IEEE J. Select. Top. Quantum Electron.* **18**, 399–410.

Miao, J., Sayre, D. & Chapman, H. N. (1998). *J. Opt. Soc. Am. A*, **15**, 1662–1669.
Nakamura, R., Lee, J.-G., Mori, H. & Nakajima, H. (2008). *Philos. Mag.* **88**, 257–264.
Petersen, J. & Mayr, S. G. (2008). *J. Appl. Phys.* **103**, 023520.
Railsback, J. G., Johnston-Peck, A. C., Wang, J. & Tracy, J. B. (2010). *ACS Nano*, **4**, 1913–1920.
Rellinghaus, B., Stappert, S., Wassermann, E. F., Sauer, H. & Spliethoff, B. (2001). *Eur. Phys. J. D*, **16**, 249–252.
Robinson, I., Clark, J. & Harder, R. (2016). *J. Opt.* **18**, 054007.
Smigelskas, A. D. & Kirkendall, E. O. (1947). *Trans. AIME*, **171**, 130.
Song, P., Wen, D., Guo, Z. X. & Korakianitis, T. (2008). *Phys. Chem. Chem. Phys.* **10**, 5057–5065.
Takahashi, Y., Zettsu, N., Nishino, Y., Tsutsumi, R., Matsubara, E., Ishikawa, T. & Yamauchi, K. (2010). *Nano Lett.* **10**, 1922–1926.
Thibault, P., Dierolf, M., Menzel, A., Bunk, O., David, C. & Pfeiffer, F. (2008). *Science*, **321**, 379–382.
Thibault, P., Elser, V., Jacobsen, C., Shapiro, D. & Sayre, D. (2006). *Acta Cryst.* A**62**, 248–261.
Yin, Y., Rioux, R. M., Erdonmez, C. K., Hughes, S., Somorjai, G. A. & Alivisatos, A. P. (2004). *Science*, **304**, 711–714.